processes

MDPI

Article

Particle Migration Mechanisms in Typical Flow Structures of an Aerospace Servo Valve

Ranheng Du, Jin Zhang *, Yiteng Shi, Ying Li, Jiahui Wu and Xiangdong Kong

School of Mechanical Engineering, Yanshan University, Qinhuangdao 066000, China; duranheng@stumail.ysu.edu.cn (R.D.); ytshi@stumail.ysu.edu.cn (Y.S.); yingli@ysu.edu.cn (Y.L.); wujiahui@stumail.ysu.edu.cn (J.W.); xdkong@ysu.edu.cn (X.K.)
* Correspondence: zhangjin@ysu.edu.cn

Abstract

Servo valves are critical components in hydraulic control systems; their performance directly affects the accuracy and reliability of systems used in aerospace and construction machinery. In service, micron-scale solid contaminants in hydraulic oil tend to deposit within the narrow clearances between spool and sleeve, causing spool sticking and accelerated wear that degrade system stability and lifetime. This study combines fluid–particle coupling analysis, numerical simulation, and experiments to examine particle motion and migration in representative valve-like flow fields. A force model for particles in viscous hydraulic oil is derived from fluid- and particle-dynamics principles, and two-dimensional CFD–DPM models are constructed for laminar, jet-like, and swirling flow conditions. Parametric simulations explore the influence of flow velocity, particle size, and particle density on particle trajectories and displacement. Results indicate that particle size has the strongest effect on migration behavior, with particle displacement increasing from 0.35% to 30.65% in laminar flow, from 2.31% to 67.08% in jet-like flow, and from 1.93% to 145.09% in swirling flow. Fluid velocity also significantly affects particle displacement, while particle density has a relatively minor influence. Swirling flow produces the largest displacement, followed by jet-like and laminar flow. Finally, a Particle Image Velocimetry (PIV)–style experimental platform on scaled models is used to validate key simulation trends. Findings clarify dominant mechanisms of particle contamination in servo valves and offer guidance for gap optimization and anti-contamination design.

Keywords: servo valve; solid particle contamination; fluid-particle coupling; dynamic mechanism; Particle Image Velocimetry (PIV) experiment

Check for updates

Academic Editor: Krzysztof Rogowski

Received: 6 March 2026
Revised: 21 April 2026
Accepted: 24 April 2026
Published: 28 April 2026

Copyright: © 2026 by the authors. Licensee MDPI, Basel, Switzerland. This article is an open access article distributed under the terms and conditions of the Creative Commons Attribution (CC BY) license.

1. Introduction

Fuel electro-hydraulic servo valves are critical actuating components in modern hydraulic control systems, with their performance directly influencing the reliability and precision of aerospace and other high-demand equipment. Among various valve core designs, the spool valve is widely adopted due to its favorable guiding characteristics and ease of installation [1]. In practical operation, fluid contamination is implicated in over 75% of hydraulic system failures, with valve sticking and wear caused by solid particles representing persistent challenges in hydraulic engineering [2–4]. The clearance between the spool and valve body serves dual purposes: it provides a lubricating oil film to prevent direct metal contact, and it stabilizes spool movement by balancing pressure [5]. When solid contaminants enter the clearance with the flowing fluid, most particles are carried out

by the main stream at the outlet, but a fraction remains trapped within the clearance. These retained particles increase the spool's sticking resistance, adversely affecting its dynamic behavior [6,7].

In terms of the forces acting on particles within the flow field, scholars have made a series of breakthroughs. Daghooghi et al. compared irregularly shaped particles with their equivalent spheres, showing that two geometric factors of irregular shapes are related to particle stress [8]. Terrell et al. developed a motion trajectory model for solid particles by combining the continuous medium model and particle dynamics, and calculated the trajectories of nanometer-sized solid particles in abrasive fluids [9]. Romero-Valle et al. proposed a new model for calculating the drag and resistance torque of non-spherical particles, which can accurately predict both the rotational and translational motion of non-spherical particles [10]. Fedina et al. studied the motion behavior of different shapes of particles in powder beds [11]. Naghashnejad et al. used computational fluid dynamics (CFD) to solve the three-dimensional conservation equations of mass and momentum on polyhedral grids using the finite volume method, providing drag coefficient correlations that can help reduce fluid dynamic resistance caused by irregularly shaped particles [12].

The analysis of liquid–solid two-phase flow provides an important research tool for revealing the dynamic behavior of particles in the clearance. Robinson et al. proposed a mesh-free simulation method based on particles to model multiphase flow of particles, offering a new computational approach for particle motion studies [13]. Ebrahimi et al. conducted a comparative analysis of two major two-phase flow modeling methods [14]. Kandlikar et al. investigated a microscale channel system with a relative roughness of up to 14%, demonstrating that such wall roughness can significantly affect unidirectional flow characteristics and pressure drop, which in turn may influence particle motion in narrow gaps [15]. Tic et al. analyzed the particle motion in a hydraulic oil tank under transient conditions based on two-phase flow computational methods [16]. Elaswad et al. employed a discrete particle model to simulate the motion of solid particles with varying sizes in an accelerating annular membrane, providing a basis for future research and potential applications in particle imaging velocimetry (PIV) gyroscopes [17]. Pomeroy P. E. and Vaughan N. D. from the University of Bath, UK, developed a multi-parameter coupled dynamic testing platform to achieve a quantitative assessment of erosion damage on the spool–sleeve assembly under controlled flow field conditions [18,19]. Edwards J. K., and Frawley P. investigated erosion and wear phenomena in pipeline systems using numerical simulation methods [20,21].

In recent years, numerous studies have investigated the forces acting on solid particles and their motion characteristics in internal flow fields. Most existing work relies on theoretical analysis or numerical simulation techniques to describe particle behavior. However, for hydraulic servo valves, the internal flow structures are complex and vary significantly with operating conditions, and the corresponding particle motion characteristics have not yet been fully clarified. In particular, the influence of different representative flow states—such as flows dominated by laminar characteristics, jet effects, or swirling motion—on particle migration inside valve clearances has received limited attention. Although three-dimensional CFD simulations are increasingly used in engineering analysis, simplified two-dimensional models are still commonly adopted in preliminary studies to extract dominant physical mechanisms and to facilitate experimental observation and interpretation. Based on this background, the present study focuses on the particle migration behavior in valve-like flow passages under different typical flow states by combining simplified force analysis, two-dimensional numerical modeling, and experimental visualization. The purpose of this work is to provide a physically intuitive understanding of particle motion mechanisms in hydraulic valves, rather than to substitute comprehensive three-dimensional

CFD analyses. The main novelties of this work are threefold. First, a particle force analysis framework is established for representative valve-like flow fields in viscous hydraulic oil. Second, three typical flow-field patterns, namely laminar, jet-like, and swirling flows, are used to extract general particle migration characteristics in spool–sleeve clearances, and the effects of particle size, fluid velocity, and density are systematically compared. Third, the main numerical findings are supported by experimental flow visualization on scaled models.

This paper focuses on the motion behavior of solid particles under different flow field conditions inside a fuel electro-hydraulic servo valve. In Section 2, the forces acting on particles in different flow fields are analyzed using liquid-solid two-phase flow research methods. Section 3 analyzes the flow patterns in three flow models. Section 4 discusses the influence of different factors on the particle deviation characteristics in the three flow models. To verify the accuracy of the simulation model, experimental validation is conducted in Section 5. Section 6 concludes the paper.

2. Particle Force Analysis

2.1. The Effect of Particles on the Spool Valve

Figure 1a presents the schematic diagram of a servo valve, which typically comprises three main components: the torque motor, the hydraulic amplifier, and the feedback mechanism. Particle contamination is inevitably present in the servo valve's working system. If excessive particles migrate and accumulate in the internal clearance, these sensitive particles can cause friction and wear on the spool surface during the spool's operation. This directly affects the performance and service life of the hydraulic system and may even lead to spool jamming, resulting in the failure of hydraulic components and disrupting the normal operation of the system. Figure 1b illustrates the motion of particles in the valve chamber.

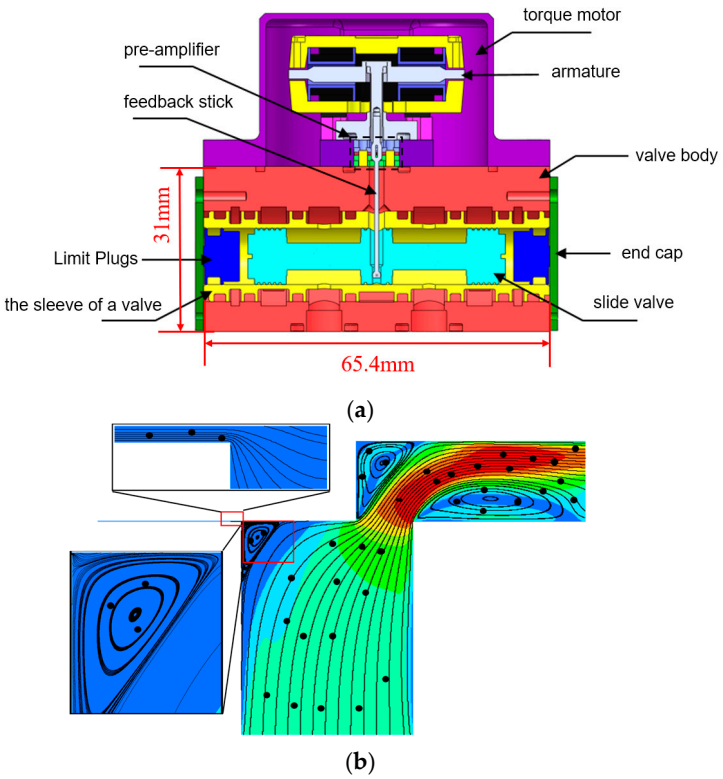


Figure 1. Schematic diagram of internal structure of fuel electro-hydraulic servo valve. (**a**) Schematic diagram of the servo valve; (**b**) Schematic of particle motion in the valve chamber.

2.2. Establishment of Particle Motion Models Under Different Flow States

(1) Establishment of particle motion model under laminar flow conditions

Based on the simplified force analysis of the particles, under laminar flow conditions, The motion of a single particle is governed by Newton's second law, considering gravity, buoyancy, and drag forces, which can be expressed as follows [22]: the equation of motion for solid particles is

$$m_p \frac{\partial u_p}{\partial t} = F_G + F_f + F_D \quad (1)$$

where m_p—The mass of a single particle (kg);
u_p—The velocity of a single particle (m/s);
t—Particle motion time (s);
F_G—The gravity of the particle (N);
F_f—Buoyancy force on the particle (N);
F_D—Drag force on the particle (N);

The relative velocity between the particle and the surrounding fluid can be obtained by balancing gravity, buoyancy, and drag forces [23]:

$$u_p^{\infty} = u_L + \sqrt{\frac{4}{3}\frac{d_p}{C_D}\frac{\rho_p - \rho_L}{\rho_L}g} \quad (2)$$

where u_p—the velocity of a single particle (m/s);
u_L—Instantaneous velocity of the fluid (m/s).
d_p—Particle diameter (m).
C_D—Drag coefficient;
g—Gravitational acceleration(m/s^2);
ρ_p—Particle density (kg/m^3).
ρ_L—Fluid density (kg/m^3).

The formula is valid under laminar flow conditions, where the Reynolds number is approximately below 2320. The terminal velocity of the particle is influenced by the fluid velocity, drag coefficient, particle diameter, and density difference. An increase in particle diameter, fluid velocity, and density difference leads to a higher terminal velocity. Conversely, an increase in the drag coefficient and fluid density results in a lower terminal velocity. The terminal velocity determines the particle's deviation characteristics: the higher the velocity, the stronger the inertia, and the more likely the particle is to deviate from the streamline; the lower the velocity, the drag force dominates, and the particle moves more closely along the streamline. Therefore, parameters such as particle diameter, fluid velocity, and density difference directly affect the degree of lateral deviation.

(2) Establishment of particle motion model under non-laminar flow conditions

Based on the simplified force analysis, it can be concluded that under non-laminar conditions, the main forces acting on the particles include gravity, buoyancy, drag force, pressure gradient force, inertial force, added mass force, Magnus force, Basset force, and Saffman force. The equation of motion for solid particles is [24]

$$m_p \frac{\partial u_p}{\partial t} = F_G + F_f + F_P + F_D + F_I + F_a + F_B + F_M + F_S \quad (3)$$

where m_p—The mass of a single particle (kg);
u_p—The velocity of a single particle (m/s);
t—Particle motion time (s);
F_G—The gravity of the particle (N);

F_f—Buoyancy force on the particle (N);
F_P—Pressure gradient force on the particle (N);
F_D—Drag force on the particle (N);
F_I—Inertial force on the particle (N);
F_a—Added mass force on the particle (N);
F_B—Basset force on the particle (N);
F_M—Magnus force on the particle (N);
F_S—Saffman force on the particle (N).

The particle diameter and density difference determine the magnitudes of gravity and buoyancy. The larger the diameter, the greater the particle volume and mass, and consequently, the larger the gravitational force on the particle. The greater the difference between the particle density and the fluid density, the more significant the effect of buoyancy. The fluid's density and viscosity directly influence the drag and added mass forces. When the fluid density is higher, the drag and added mass forces increase, thus hindering particle motion; when the fluid viscosity is higher, it impedes changes in particle velocity.

The numerical simulation in this study was performed using a CFD framework. For the continuous phase, the flow field of hydraulic oil was governed by the continuity equation and the momentum equation. Since the hydraulic oil was treated as an incompressible fluid, the continuity equation can be written as

$$\nabla \cdot \mathrm{u} = 0 \tag{4}$$

The momentum equation is expressed as

$$\rho(\partial \mathrm{u}/\partial \mathrm{t} + \mathrm{u} \cdot \nabla \mathrm{u}) = -\nabla \mathrm{p} + \mu \nabla^2 \mathrm{u} + \rho \mathrm{g} \tag{5}$$

where u is the fluid velocity vector, p is the pressure, ρ is the fluid density, μ is the dynamic viscosity, and g is the gravitational acceleration.

3. Flow Model Establishment and Flow Field Analysis

3.1. Flow Model Establishment

Under different flow field conditions, factors such as the fluid velocity and the physical properties of the particles will influence the forces acting on the particles and their motion behavior. Due to the extremely complex flow within the spool valve chamber, which involves various flow states such as laminar flow, jet flow, and vortex flow, it is very challenging to directly analyze the particle behavior inside the valve. The flow states within the spool valve chamber can primarily be categorized into laminar flow, vortex flow, and jet flow, as shown in Figure 2.

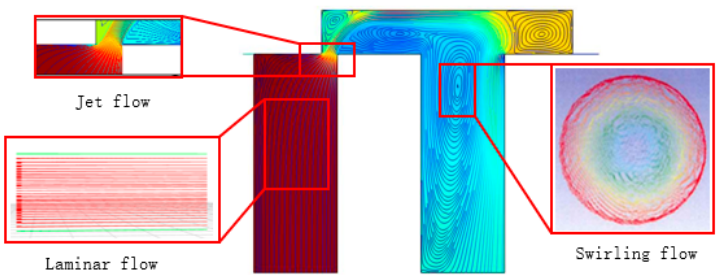


Figure 2. Schematic diagram of flow in the spool valve chamber.

To simulate the motion behavior of particles under three different flow conditions, a two-dimensional laminar flow field model, jet flow field model, and vortex flow field

model are established, as shown in Figure 3. The 2D simplification facilitates capturing dominant flow features and migration trends but does not account for three-dimensional wall confinement, spanwise variations, or secondary flows induced by moving spool geometries. Consequently, quantitative differences between 2D predictions and true 3D valve flows can be expected—particularly for local interface details—but the 2D approach remains useful for identifying regime-dependent behavior and parameter sensitivities (flow speed, particle size, density).

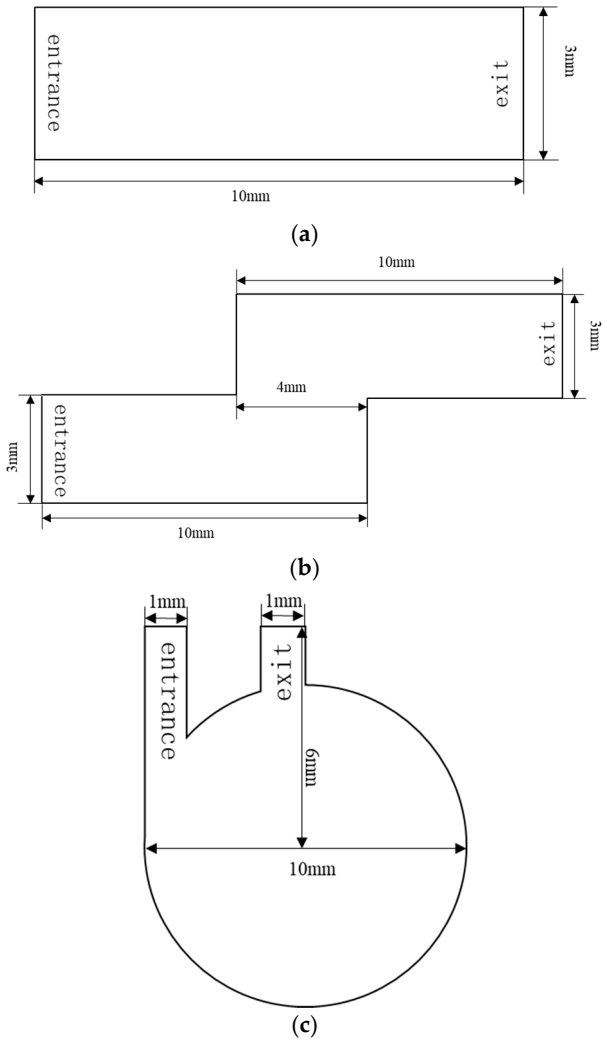


Figure 3. Two-dimensional flow field model. (**a**) Two-dimensional laminar flow model; (**b**) Two-dimensional jet flow model; (**c**) Two-dimensional vortex flow model.

3.2. Mesh Generation and Boundary Condition Setup

Mesh generation is a key step in the discretization of the governing equations and has an important influence on numerical accuracy, convergence, and computational efficiency. In the present study, structured meshes were employed for the laminar and jet-like flow models because of their relatively simple geometries, whereas an unstructured mesh was adopted for the swirling flow model to better accommodate its more complex geometry and local flow features. Before the formal calculations, mesh quality was evaluated using standard quality indicators, including skewness and orthogonal quality, and the generated meshes satisfied the solver requirements for numerical stability and accuracy.

To ensure that the numerical results were independent of mesh size, a grid independence study was carried out for the laminar, jet-like, and swirling flow models. Five global

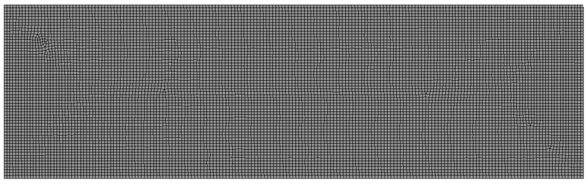
mesh sizes, namely 0.01, 0.03, 0.05, 0.07, and 0.1 mm, were tested under identical boundary conditions. The final longitudinal coordinates of representative trajectories starting from the same initial position were selected as the comparison criterion. As shown in Table 1, the variations in the final longitudinal coordinates are very small for all three models, indicating that the numerical results have essentially reached grid independence. Considering the balance between numerical accuracy and computational efficiency, a global mesh size of 0.05 mm was finally selected for all three models.

Table 1. Final longitudinal trajectory coordinates for different mesh sizes.

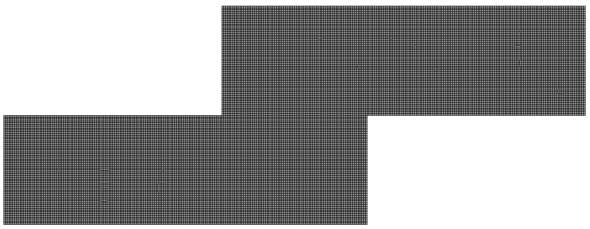
No.	Mesh Size (mm)	Laminar Flow (mm)	Jet-like Flow (mm)	Swirling Flow (mm)
1	0.01	1.499833	4.439885	4.399775
2	0.03	1.499827	4.439898	4.399853
3	0.05	1.499826	4.439915	4.399899
4	0.07	1.499824	4.439900	4.399878
5	0.1	1.499825	4.439899	4.399885

The continuous phase was solved using a pressure-based solver, and the pressure–velocity coupling was handled using the SIMPLE algorithm. Second-order spatial discretization schemes were adopted to improve numerical accuracy. The particle trajectories were calculated after the convergence of the continuous phase. Convergence was assessed based on both residual reduction and the stabilization of monitored physical quantities. The solution was considered converged only when the residuals reached the prescribed criterion and the key monitored variables no longer changed noticeably with further iterations.

For the laminar and jet flow models established in this section, structured grids are used for the laminar and jet flow models based on the structural adaptability, while unstructured grids are employed for the vortex flow model to accommodate different geometric structures and boundary layer regions. The grid generation for the models is shown in Figure 4. The mesh generation parameters are shown in Table 2.

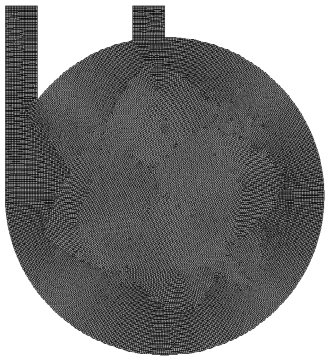


(**a**)



(**b**)

Figure 4. *Cont.*



(c)

Figure 4. Flow field model mesh generation. (**a**) Laminar flow model mesh generation; (**b**) Jet flow model mesh generation; (**c**) Vortex flow model mesh generation.

Table 2. Mesh generation parameter table.

Flow Field Model	Cell Size	Number of Grids	Number of Nodes	Minimum Mesh Quality	Maximum Mesh Quality	Average Mesh Quality
Laminar flow	0.05	11,234	11,479	0.60426	0.99947	0.98841
Jet flow	0.05	24,000	24,441	0.97833	0.99947	0.99904
Vortex flow	0.05	33,555	33,887	0.41992	0.99962	0.93382

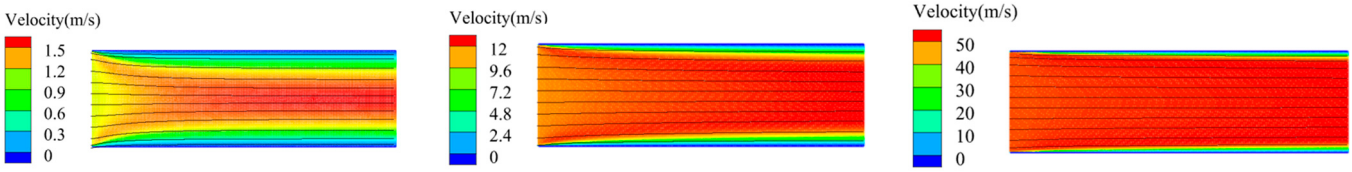
The laminar flow model was numerically simulated using analytical software. The entire model assumes the fluid to be incompressible and Newtonian, with constant density and viscosity, and the flow state satisfies steady-state conditions, which means that the velocity and pressure fields in the flow field remain unchanged over time. The oil used is anti-wear hydraulic oil with a viscosity grade of 46, which is a standard hydraulic oil commonly used in industrial applications and in hydraulic simulations, at room temperature, with a density of 871 kg/m^3 and a dynamic viscosity of 0.04 Pa·s. The boundary conditions are set as a velocity inlet and a free-flow outlet. The flow field velocity is a key factor influencing the forces acting on the particles, and thus their adherence to the oil flow. Therefore, five operating conditions for the inlet velocity ranging from 0.1 to 50 m/s were considered to explore the effects of different flow fields on particle motion. The wall was set with a no-slip boundary condition, and the velocity at the fluid-wall contact was set to zero. The specific parameters are shown in Table 3.

Table 3. Flow field boundary condition parameter table.

Parameter	Unit	Value
Density of oil	kg/m^3	871
Fluid dynamic viscosity	Pa·s	0.04
Inlet velocity	m/s	1, 10, 50
Outlet boundary condition setup	m/s	Outflow

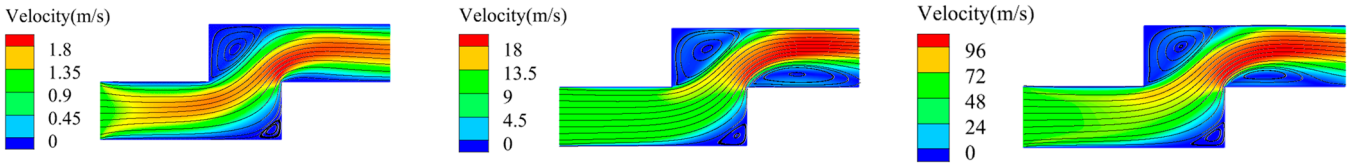
3.3. Flow Field Flow Analysis

Figure 5 shows the velocity contour maps for the laminar flow field with inlet velocities of 1 m/s, 10 m/s, and 50 m/s. Figure 6 shows the velocity contour maps for the jet flow field with inlet velocities of 1 m/s, 10 m/s, and 50 m/s. Figure 7 shows the velocity contour maps for the vortex flow field with inlet velocities of 1 m/s, 10 m/s, and 50 m/s.



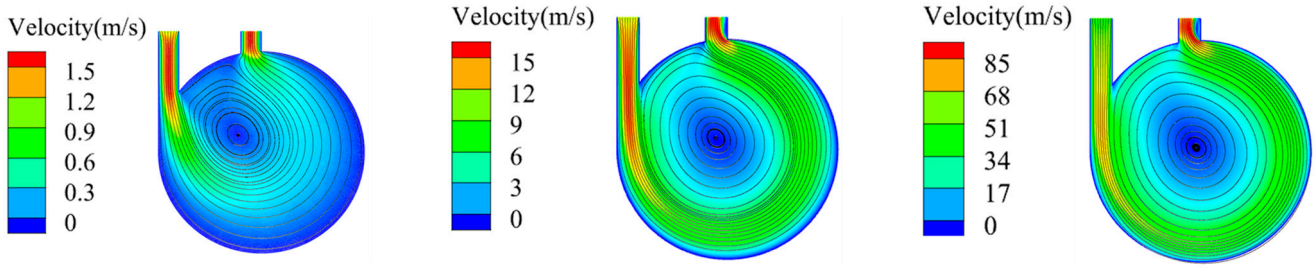
(**a**) (**b**) (**c**)

Figure 5. Laminar flow field velocity contour map. (**a**) Inlet velocity of 1 m/s; (**b**) Inlet velocity of 10 m/s; (**c**) Inlet velocity of 50 m/s.



(**a**) (**b**) (**c**)

Figure 6. Jet flow field velocity contour map. (**a**) Inlet velocity of 1 m/s; (**b**) Inlet velocity of 10 m/s; (**c**) Inlet velocity of 50 m/s.



(**a**) (**b**) (**c**)

Figure 7. Vortex flow field velocity contour map. (**a**) Inlet velocity of 1 m/s; (**b**) Inlet velocity of 10 m/s; (**c**) Inlet velocity of 50 m/s.

From the velocity contour maps in Figures 5–7, it can be seen that in the laminar flow model, as the velocity increases, the velocity near the wall drops more sharply, and high-speed flow tends to induce large velocity gradients and boundary layer separation. In the jet flow model, when the fluid passes through the corner, the flow area narrows, leading to a significant increase in velocity. A high-speed zone forms on the outer side of the bend, and a low-speed zone forms on the inner side, creating a noticeable velocity gradient. The streamlines curve at the corner, and local vortices and fluid separation occur; as the flow velocity increases, the vortices and separation zones on the inner side expand, and the vortex phenomena become more pronounced. In the vortex flow model, the fluid flows in from the inlet, forming a vortex after entry, with the velocity decreasing towards the center of the vortex, and the velocity at the center approaching zero. At low flow speeds, the vortex flow is uniform, and the velocity gradient is small; as the inlet velocity increases, the high-speed zone at the inlet becomes concentrated, the velocity gradient increases on the outer side of the circular region, and the overall stability of the flow decreases.

In summary, regardless of whether it is laminar flow, jet flow, or vortex flow in a circular region, an increase in inlet velocity will intensify the unevenness of the velocity distribution, increase the velocity gradient, and lead to phenomena such as vortices and boundary layer separation. Moreover, under high-speed flow conditions, the flow stability significantly decreases.

4. Analysis of Particle Deviation Characteristics Under Three Flow States

4.1. Particle Simulation Setup

The Discrete Phase Model (DPM) is suitable for sparse particle multiphase flow models. In general, the particle volume fraction does not exceed 10%, and the particles are treated as point masses without considering their volume. For this analysis, the DPM is selected. Based on the analysis above, particle diameter and density are crucial factors influencing particle motion. Therefore, this study primarily analyzes the following behavior of particles with different densities and diameters under different flow fields. According to the force analysis model, the main forces acting on particles in the laminar, vortex, and jet flow models include gravity, buoyancy, drag force, pressure gradient force, inertial force, added mass force, Magnus force, Basset force, and Saffman force. The gravitational acceleration is 9.81 m/s^2, and in the laminar, jet, and vortex models, the direction of gravity is perpendicular to the inlet direction.

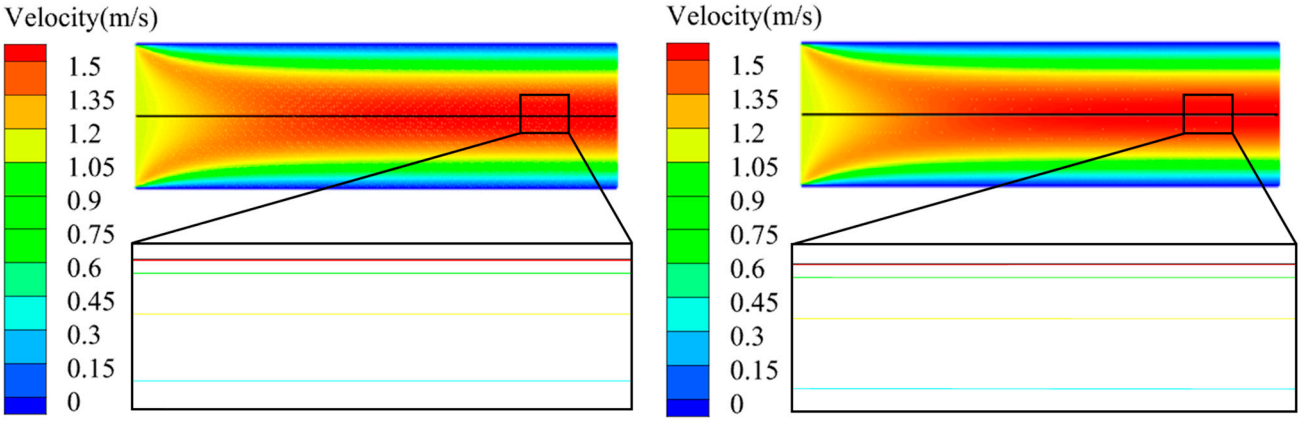
Based on the flow field simulation, the discrete particle phase calculation method is used to calculate spherical particles with different diameters and densities. According to the flow field simulation results, the velocity in the main flow region is relatively uniform. Therefore, particles are released at the center of the flow field inlet, with an initial velocity of 0 m/s. The analysis investigates particle motion under different flow velocities and density conditions, obtaining the particle deviation trajectories in the flow field. During the calculation, only the unidirectional effect of the fluid on the particles is considered, without accounting for the particles' reaction on the flow field. Specific boundary condition parameters are shown in Table 4.

Table 4. Particle boundary condition parameter table.

Parameter	Value
Particle density/(kg/m^3)	1200, 3600, 6000, 7850
Particle diameter/(μm)	1, 10, 50, 100, 150

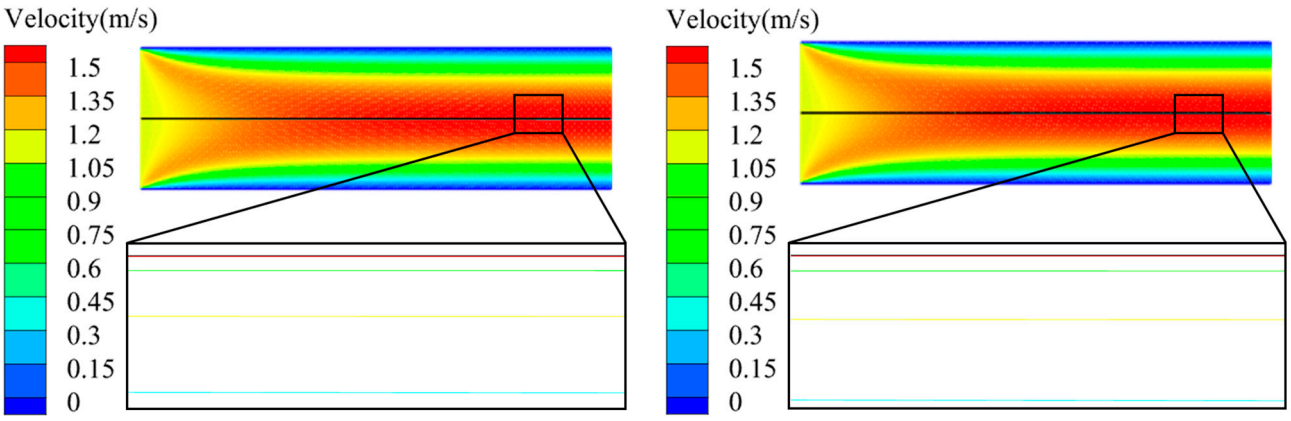
4.2. Particle Motion Trajectory Analysis

Figure 8 shows the trajectory maps of six different particle sizes under different densities in the laminar flow field at an inlet velocity of 1 m/s. The light blue represents the trajectory of 150 μm particles, yellow represents the trajectory of 100 μm particles, green represents the trajectory of 50 μm particles, red represents the trajectory of 10 μm particles, dark blue represents the trajectory of 1 μm particles, and black represents the streamline of the flow field at that point.



(**a**) (**b**)

Figure 8. *Cont.*

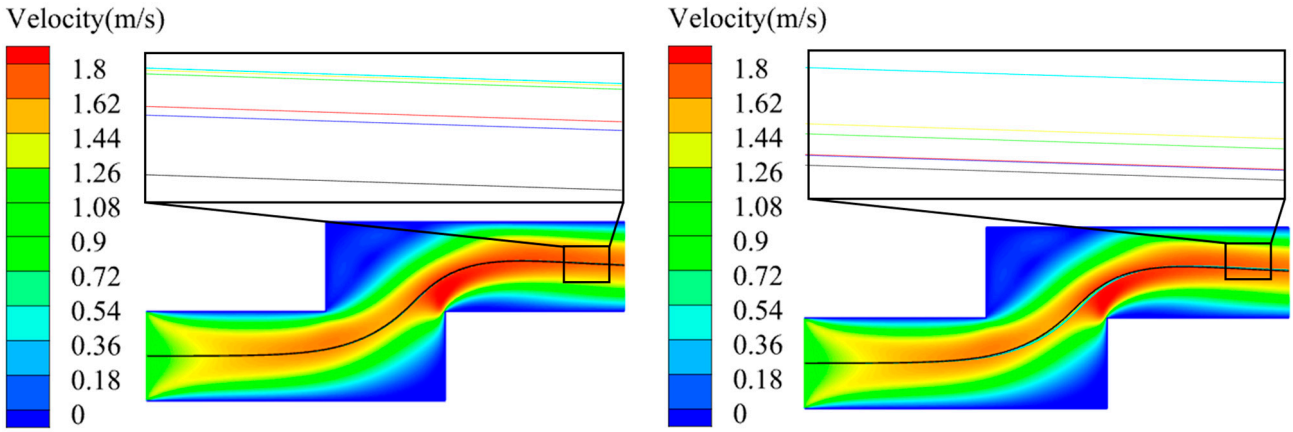


(**c**) (**d**)

Figure 8. Trajectory plots of particles with six different diameters under different densities in a laminar flow field. (**a**) Particle density of 1200 kg/m^3; (**b**) Particle density of 3600 kg/m^3; (**c**) Particle density of 6000 kg/m^3; (**d**) Particle density of 7850 kg/m^3.

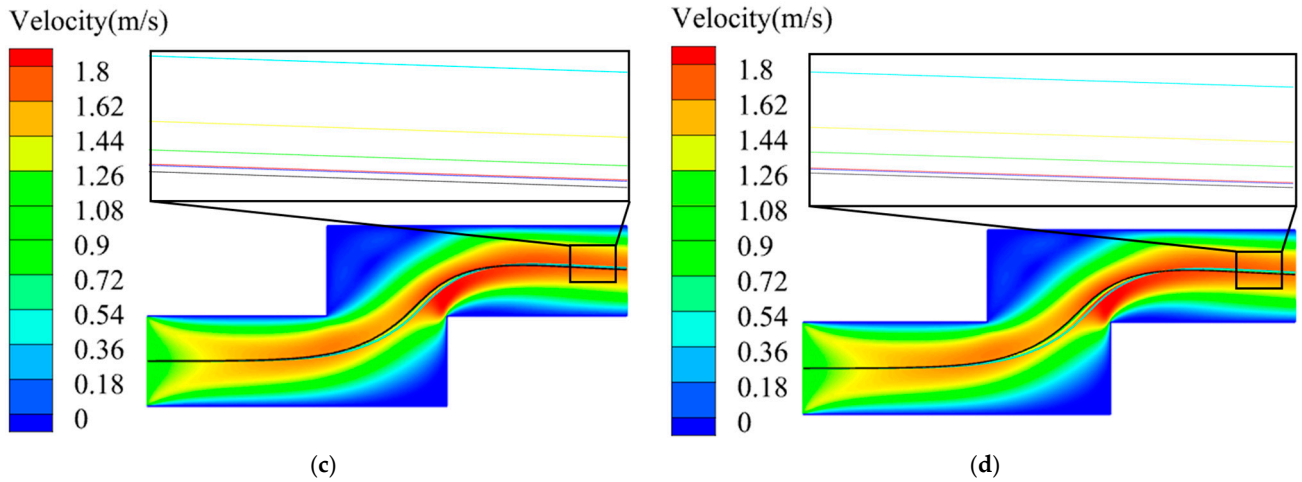
From Figure 8, it can be observed that under the same density conditions, the particle diameter has a significant impact on the deviation of its trajectory relative to the fluid. Among them, the 150 μm particles show the largest deviation, followed by the 100 μm and 50 μm particles, while the deviations of the 10 μm and 1 μm particles nearly coincide with the fluid trajectory. This indicates that particle diameter has a pronounced effect on the deviation of particles as they flow with the oil. As the particle density gradually increases, the particle deviation also increases, and under the same particle diameter conditions, the larger the particle density, the greater the deviation. This suggests that particle density has a more significant impact on larger diameter particles.

Figure 9 shows the trajectory maps of six different particle sizes under different densities in the jet flow field at an inlet velocity of 1 m/s. The light blue represents the trajectory of 150 μm particles, yellow represents the trajectory of 100 μm particles, green represents the trajectory of 50 μm particles, red represents the trajectory of 10 μm particles, dark blue represents the trajectory of 1 μm particles, and black represents the streamline of the flow field at that point.



(**a**) (**b**)

Figure 9. *Cont.*

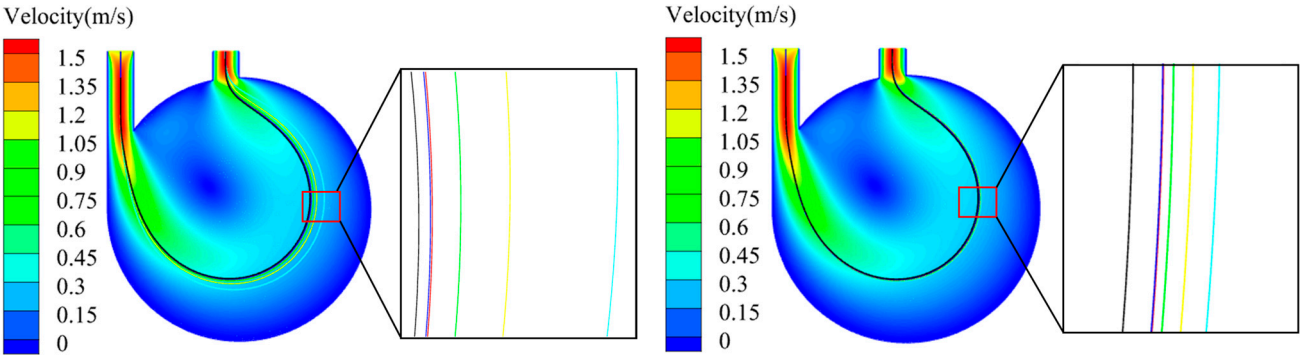


(**c**) (**d**)

Figure 9. Trajectory plots of particles with six different diameters under different densities in a jet flow field. (**a**) Particle density of 1200 kg/m^3; (**b**) Particle density of 3600 kg/m^3; (**c**) Particle density of 6000 kg/m^3; (**d**) Particle density of 7850 kg/m^3.

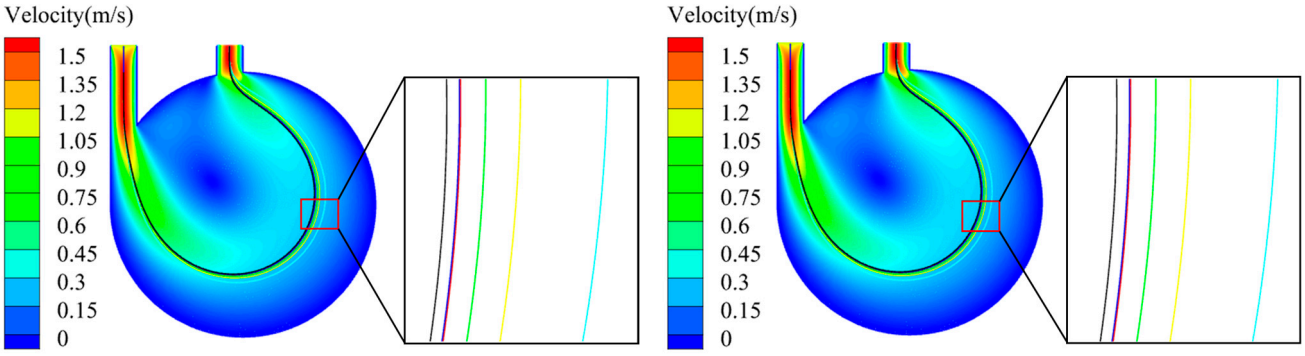
As shown in Figure 9, under the same density conditions, particle size has a significant effect on the displacement relative to the fluid trajectory. Among these, the 150 μm particles exhibit the largest displacement, significantly greater than that of other particle sizes, while the displacement of the 10 μm and 1 μm particles almost coincides with the fluid trajectory. This indicates that particle size has a notable impact on the deviation of particles as they flow with the oil. When the particle density further increases, the displacement of the 150 μm particles shows a very obvious upward trend, while the displacement of other particles also increases with density, but the rate of change is much smaller than that of the 150 μm particles. This suggests that larger particles are more sensitive to density variations in the jet flow field. As the particle density gradually increases, the particle displacement also increases. Furthermore, under the same particle size condition, the larger the particle density, the greater the displacement, indicating that particle size has a more pronounced effect on larger particles.

Figure 10 shows the trajectories of six different particle sizes at different densities when the inlet velocity in the swirl flow field is 1 m/s. The light blue represents the trajectory of 150 μm particles, yellow represents the trajectory of 100 μm particles, green represents the trajectory of 50 μm particles, red represents the trajectory of 10 μm particles, dark blue represents the trajectory of 1 μm particles, and black represents the streamline of the flow field at that point.



(**a**) (**b**)

Figure 10. *Cont.*



(**c**) (**d**)

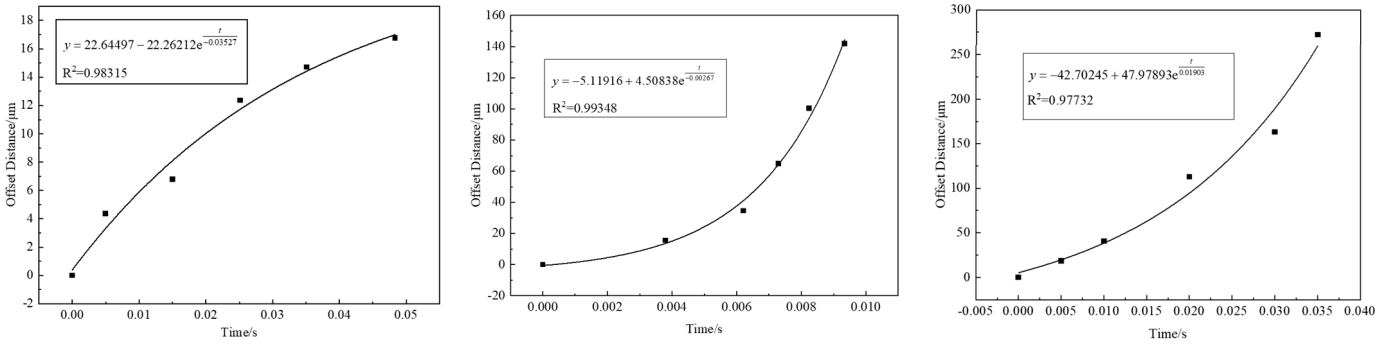
Figure 10. Trajectory of particles with six different sizes at varying densities in a swirling flow field. (**a**) Particle density of 1200 kg/m^3; (**b**) Particle density of 3600 kg/m^3; (**c**) Particle density of 6000 kg/m^3; (**d**) Particle density of 7850 kg/m^3.

As shown in Figure 10, under the swirling flow condition, the particle displacement pattern is similar to that of the jet flow. When the particle density is 1200 kg/m^3, particles of different sizes exhibit a certain degree of displacement relative to the fluid trajectory, and the displacement distance gradually increases with the particle size. Especially for particles with a size of 150 μm, the displacement is significantly larger than that of other particle sizes. As the particle density increases, the displacement distance also increases with the density.

4.3. Influence of Different Factors on Particle Displacement Characteristics

When particles move with the flow field, their trajectories relative to the flow field are affected by changes in the flow field as well as by the particle's inertia and other factors. A streamline represents the path traced by a fluid particle moving through space. The tangent direction of the streamline indicates the velocity direction of the same fluid particle at different times. A streamline represents the flow trajectory of a single particle over a continuous period of time, and is one of the Lagrangian methods used to describe the flow. To investigate the ability of particles to follow the flow field, the distance between the coordinates of the particles and the streamlines at the same moment is defined as the displacement distance.

Figure 11 shows the variation in particle displacement distance over time (t) in laminar flow, jet flow, and swirling flow fields when the particle size is 0.01 mm, particle density is 7850 kg/m^3, and the flow field velocity is 1 m/s.



(**a**) (**b**) (**c**)

Figure 11. Variation in particle displacement with time. (**a**) Laminar Flow Field; (**b**) Jet Flow Field; (**c**) Swirling Flow Field.

Figure 11 reveals the variation in particle displacement distance over time in three typical flow fields (laminar, jet, and swirling) for particles with a diameter of 0.01 mm and a density of 7850 kg/m^3. The displacement–time relationship of the particles is fitted using an exponential function, and the coefficient of determination for all three flow fields is greater than 0.97. The fitting equations can effectively predict the trend of particle displacement.

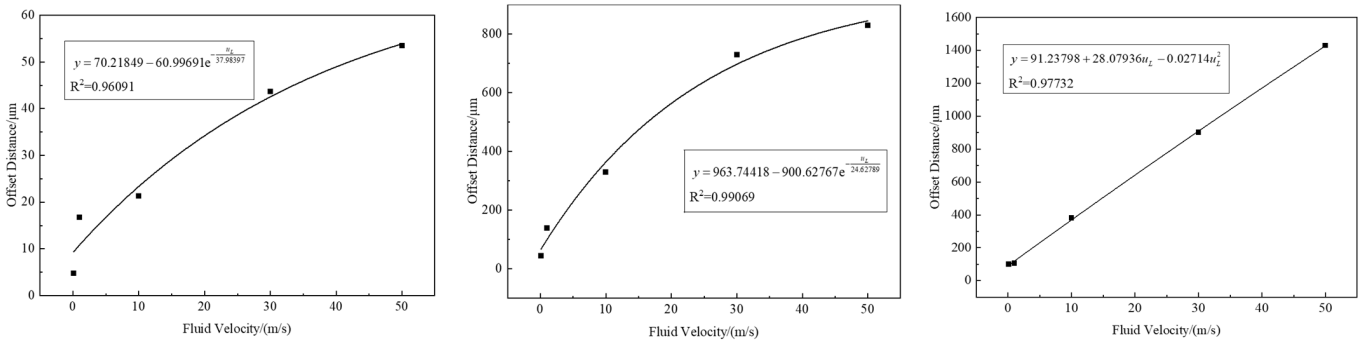
In the laminar flow state, the particle displacement distance increases non-linearly over time. In the initial stage, the particle displacement grows rapidly, but the rate of growth gradually slows down, with the displacement reaching approximately 18 μm at 0.05 s. This change is mainly due to the larger velocity difference between the particles and the fluid in the initial phase under laminar flow, resulting in accelerated displacement growth and greater fluid drag force. As time progresses, the particle speed increases gradually, the difference between the particle speed and the flow field speed decreases, and the drag force diminishes, which leads to a reduction in the rate of displacement increase.

In the jet flow state, the particle displacement distance exhibits an exponential growth trend over time. For times less than 0.004 s, the displacement increases slowly, as the particles are initially in regions with lower flow velocities, experiencing smaller drag forces, and moving at a slower speed. However, between 0.004 and 0.010 s, the particles reach the throttling zone, where the flow velocity increases, and the drag force, inertial force, and added mass force rapidly increase, leading to a rapid increase in displacement. As the velocity increases, the particle displacement continues to grow, reaching approximately 150 μm at 0.010 s.

In the swirling flow state, the particle displacement distance shows a curvilinear growth pattern over time. The displacement gradually increases, reaching about 250 μm at 0.035 s, and the rate of increase is notably higher than in the laminar and jet flow states. This is because in the swirling state, the centrifugal force further drives the particles away from their original trajectory. Additionally, the vortex structure in the swirling flow also has an impact on the particle displacement.

In conclusion, the variation in particle displacement with time differs across various flow states: in the laminar state, the displacement increases relatively slowly; in the jet state, the displacement increases rapidly; and in the swirling state, the displacement grows the fastest.

Figure 12 shows the variation in particle displacement distance with fluid velocity u_L for particles with a size of 0.01 mm and a density of 7850 kg/m^3 in laminar, jet, and swirling flow fields.



(**a**) (**b**) (**c**)

Figure 12. Effect of fluid velocity on particle displacement. (**a**) Laminar Flow Field; (**b**) Jet Flow Field; (**c**) Swirling Flow Field.

Figure 12 illustrates the influence of fluid velocity on particle displacement. The relationship between particle displacement and fluid velocity was fitted using exponential or polynomial power functions, and the coefficient of determination for each model is

greater than 0.96, indicating that the fitting equations can effectively predict the trend of particle displacement.

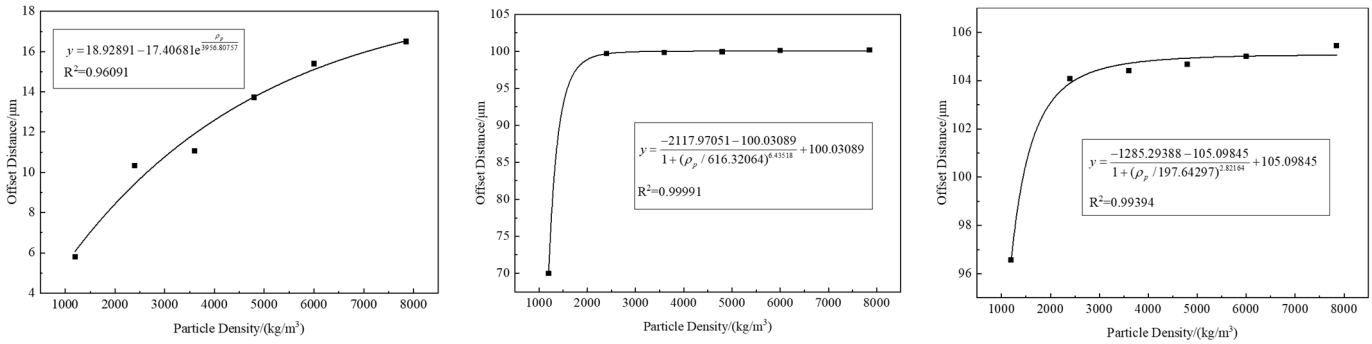
In the laminar flow state, the particle displacement distance increases non-linearly with the fluid velocity. In the low-velocity region, the displacement grows slowly, but once the velocity exceeds 20 m/s, the rate of displacement increase significantly accelerates and stabilizes in the high-velocity region. In the laminar state, particles are primarily influenced by fluid drag and gravity. This suggests that, under laminar conditions, the fluid drag on the particles increases with velocity, but the rate of increase is relatively small.

In the jet flow state, the particle displacement distance increases non-linearly with fluid velocity. The displacement changes significantly in the low-velocity region, and in the high-velocity region, the displacement reaches higher values. The increase in fluid velocity in the jet state notably enhances turbulent kinetic energy, resulting in a stronger inertial effect on the particles. Additionally, the pressure gradient in the flow field is more pronounced in the jet state, and the forces due to pressure gradient, added mass, and other factors increase with velocity, driving the particles away from their streamline trajectories and significantly increasing the displacement. Furthermore, the pulsation effects in the turbulent flow enhance the non-uniformity of the forces on the particles, especially contributing to the displacement of particles in the mid-to-high velocity range.

In the swirling flow state, the particle displacement distance increases nearly linearly with the fluid velocity. When the velocity reaches 50 m/s, the displacement reaches around 1400 μm, which is significantly higher than the other two flow states. In the swirling state, particles are influenced not only by fluid drag and inertial forces but also by substantial centrifugal forces. As the fluid velocity increases, the flow field becomes more complex, and the centrifugal force increases, making the particle motion more unstable and significantly increasing the displacement. This phenomenon becomes more pronounced at higher flow field velocities.

In summary, for all three flow states, the particle displacement relative to the flow field's trajectory increases with fluid velocity, although the trend varies between flow fields. The displacement in the swirling flow field is particularly pronounced, nearly linear in nature, and the displacement distance is much larger compared to the other two flow states.

Figure 13 shows the variation in particle displacement distance with particle density ρ_p for particles with a diameter of 0.01 mm and a fluid velocity of 1 m/s in laminar, jet, and swirling flow fields.



(**a**) (**b**) (**c**)

Figure 13. Effect of particle density on particle displacement. (**a**) Laminar Flow Field; (**b**) Jet Flow Field; (**c**) Swirling Flow Field.

Figure 13 reveals the influence of particle density on particle displacement characteristics. The relationship between particle displacement distance and density was fitted using an exponential function, and the coefficient of determination for all models is greater

than 0.96, indicating that the fitting equations can effectively predict the trend of particle displacement.

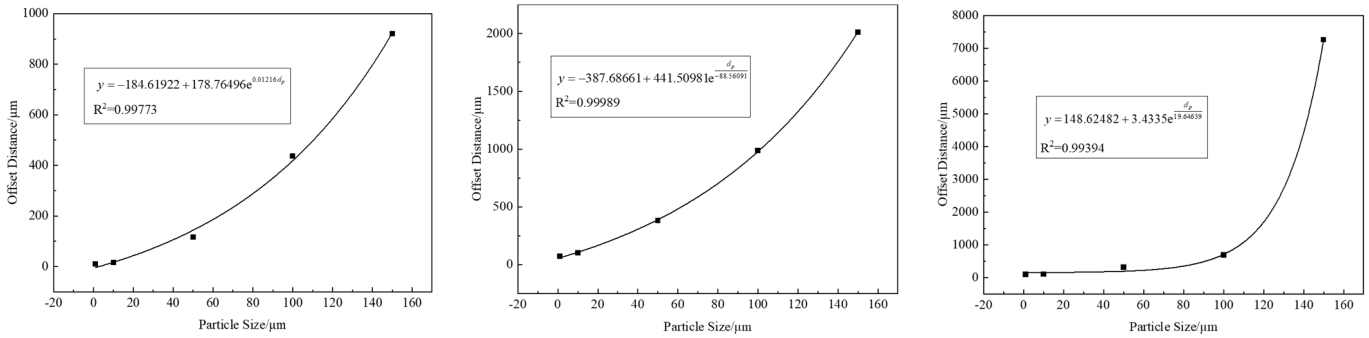
In the laminar flow state, the particle displacement distance increases gradually with density, showing a nonlinear increasing trend. The curve exhibits an approximate exponential growth, with the displacement increasing slowly in the lower-density region. However, as the density increases, the displacement gradually increases and eventually tends to saturate in the high-density region. In this state, the particle motion is primarily influenced by both fluid drag and inertial forces. At higher densities, the inertial force dominates, leading to an increase in displacement.

In the jet flow state, the particle displacement distance increases with increasing density and stabilizes once the density reaches a certain value. The growth of displacement for particles with lower densities is notably higher than in the laminar state, suggesting that the jet flow field has an enhancing effect on particle displacement. When the density exceeds 3000 kg/m^3, the rate of displacement increase drops rapidly, and the displacement remains below 102 μm.

In the swirling flow state, the trend of particle displacement with increasing density is similar to that in the jet state, where the displacement increases rapidly with density and eventually tends to saturate after reaching a certain density. In the low-density region, the increase in displacement is significantly higher than in the laminar state, indicating that the high-speed motion in the swirling flow field has a pronounced enhancing effect on particle displacement. Furthermore, the overall displacement distance in the swirling state is higher than in the jet state. The presence of rotational effects in the flow field significantly increases the centrifugal force acting on the particles, showing that the swirling flow state exerts a stronger driving force on particle displacement.

In summary, the influence of the three flow field types on particle displacement behavior is significantly different: in the laminar state, particle displacement is relatively weak, with the displacement showing a clear change with density. In the jet and swirling states, there is a stronger effect on low-density particles, showing a faster growth trend. However, once the particle density exceeds 2000 kg/m^3, the displacement distance remains almost unchanged.

Figure 14 shows the variation in particle displacement distance with particle size d_p for particles with a density of 7850 kg/m^3 and a fluid velocity of 1 m/s in laminar, jet, and swirling flow fields.



(**a**) (**b**) (**c**)

Figure 14. Effect of particle size on particle displacement. (**a**) Laminar Flow Field; (**b**) Jet Flow Field; (**c**) Swirling Flow Field.

Figure 14 reveals the influence of particle size on particle displacement characteristics. The relationship between particle displacement distance and fluid velocity was fitted using an exponential function, and the coefficient of determination for each model is greater

than 0.99, indicating that the fitting equations can effectively predict the trend of particle displacement.

Under laminar flow conditions, the particle displacement distance increases non-linearly with particle size. As shown in Figure 14a, when the particle size is 40 μm, the displacement is approximately 200 μm; when the particle size increases to 160 μm, the displacement increases to approximately 900 μm. This growth trend is relatively slow, suggesting that under laminar conditions, the forces acting on the particles are more uniform. As the particle size increases, the gravitational force on the particles also increases, leading to a gradual increase in displacement with particle size.

Under jet flow conditions, the particle displacement distance increases non-linearly with particle size. When the particle size is 40 μm, the displacement is approximately 500 μm; when the particle size increases to 160 μm, the displacement increases to 2000 μm. This is due to the more pronounced velocity gradient in the jet flow compared to laminar flow, which increases the pressure gradient force. As the particle size increases, particles are more likely to deviate from their original trajectory due to the velocity differences.

Under swirling flow conditions, the particle displacement distance increases non-linearly and exhibits an exponential growth trend with increasing particle size. When the particle size is 40 μm, the displacement is approximately 300 μm; however, when the particle size increases to 160 μm, the displacement increases to 7000 μm, showing exponential growth. In the swirling flow condition, the displacement distance is much higher than in the laminar and jet flow states due to the centrifugal force. As the particle size increases, the centrifugal force acting on the particles also increases, especially when the particle size exceeds 100 μm, resulting in a rapid increase in displacement. Furthermore, the vortex structures in the swirling flow field cause larger particles to deviate more significantly from their original trajectories, leading to a larger displacement relative to the streamline.

The overall trend indicates that the flow state has a significant impact on particle displacement behavior: in laminar and jet flow, the displacement increases non-linearly with particle size, while in swirling flow, the displacement shows an exponential increase, especially for particles larger than 100 μm, where the displacement is much greater than for particles smaller than 100 μm.

The regression equations in Figures 12–14 are empirical representations of the observed nonlinear trends within the investigated parameter ranges and are intended for sensitivity and comparative analysis rather than as universal predictive laws. The nonlinear growth behavior is physically consistent with the particle force balance, including drag, inertia, pressure gradient, and, in the swirling case, centrifugal effects and vortex-induced transverse forces, which explain the stronger deviation observed under swirling conditions. These regressions are valid only within the studied ranges and should not be extrapolated beyond the investigated conditions.

The functional relationships for particle displacement distances under the different conditions are summarized in Table 5.

Table 5. Particle displacement function relationship under different operating conditions.

Model	Particle Density/(kg/m^3)	Particle Diameter/(μm)	Fluid Velocity/(m/s)	Particle Displacement Distance Function Relationship
Laminar Flow	7850	10	1	$y = 22.64497 - 22.26212e^{-\frac{t}{0.03527}}$
Jet Flow	7850	10	1	$y = -5.11916 + 4.50838e^{-\frac{t}{0.00267}}$
Swirling Flow	7850	10	1	$y = -42.70245 + 47.97893e^{\frac{t}{0.01903}}$

Table 5. *Cont.*

Model	Particle Density/(kg/m^3)	Particle Diameter/(μm)	Fluid Velocity/(m/s)	Particle Displacement Distance Function Relationship
Laminar Flow	7850	10	u_L	$y = 70.21849 - 60.99691e^{-\frac{u_L}{37.98397}}$
Jet Flow	7850	10	u_L	$y = 963.74418 - 900.62767e^{-\frac{u_L}{24.62789}}$
Swirling Flow	7850	10	u_L	$y = 91.23798 + 28.07936u_L - 0.02714u_L^2$
Laminar Flow	ρ_p	10	1	$y = 18.92891 - 17.40681e^{\frac{\rho_p}{3956.80757}}$
Jet Flow	ρ_p	10	1	$y = \frac{-2117.97051-100.03089}{1+\left(\rho_p/616.32064\right)^{6.43518}} + 100.0308$
Swirling Flow	ρ_p	10	1	$y = \frac{-1285.29388-105.09845}{1+\left(\rho_p/197.64297\right)^{2.82164}} + 105.0984$
Laminar Flow	7850	d_p	1	$y = -184.61922 + 178.76496e^{0.01216d_p}$
Jet Flow	7850	d_p	1	$y = -387.68661 + 441.50981e^{-\frac{d_p}{88.56091}}$
Swirling Flow	7850	d_p	1	$y = 148.62482 + 3.4335e^{\frac{d_p}{19.64639}}$

4.4. Numerical Analysis of Particle Displacement Characteristics

To perform a dimensionless analysis of the particle displacement distance, an appropriate characteristic length must be chosen for each fluid model. The dimensionless displacement is defined as η = X/Lc × 100%, where X is the particle displacement distance and Lc is the characteristic length used for normalization. In the present study, Lc denotes an actual geometric reference length of the simulation model rather than the geometric scale ratio between the experimental model and the simulation model. Specifically, the inlet length of the simulation model is taken as the characteristic length for both the laminar flow and jet-like flow models, while the swirl radius of the simulation model is used as the characteristic length for the swirling flow model. Through calculation, the displacement of particles with different particle sizes, densities, and fluid velocities in the laminar flow model was obtained. The results are shown in Table 6.

Table 6. Particle displacement in the laminar flow model.

Particle Density/(kg/m^3)	Particle Diameter/(μm)	Fluid Velocity/(m/s)	Displacement/(%)
1200	10	1	0.193642
3600	10	1	0.369000
6000	10	1	0.513358
7850	10	1	0.549837
7850	1	1	0.348667
7850	10	1	0.558479
7850	50	1	4.791793
7850	100	1	14.573000
7850	150	1	30.646667
7850	10	0.1	0.156966
7850	10	1	0.558479
7850	10	10	0.710898
7850	10	30	1.456529
7850	10	50	1.781229

Table 6 shows that under laminar flow conditions, the variation in particle density has a minor effect on the displacement. The displacement increases from 0.193642% to 0.549837%, with the overall displacement remaining below 0.6%, indicating that density has little influence on particle displacement. However, as the particle size increases, the displacement increases significantly from 0.348667% to 30.646667%, far exceeding the displacement change caused by density variation. This demonstrates the significant impact of particle size on displacement. Additionally, changes in fluid velocity also affect the particle displacement, with the displacement increasing from 0.156966% to 1.781229%, indicating that fluid velocity has a considerable influence on particle displacement.

Similarly, the displacement of particles with different particle sizes, densities, and fluid velocities in the jet flow model can be obtained, as shown in Table 7.

Table 7. Particle displacement in the jet flow model.

Particle Density/(kg/m^3)	Particle Diameter/(μm)	Fluid Velocity/(m/s)	Displacement /(%)
1200	10	1	2.332654
3600	10	1	3.327534
6000	10	1	3.336970
7850	10	1	3.339690
7850	1	1	2.308791
7850	10	1	3.339690
7850	50	1	12.634644
7850	100	1	32.845898
7850	150	1	67.078761
7850	10	0.1	1.435916
7850	10	1	4.635266
7850	10	10	10.994672
7850	10	30	24.327179
7850	10	50	27.681380

Under jet flow conditions, the variation in particle density has a minor effect on the displacement. The displacement increases from 2.332654% to 3.339690%, with the overall displacement remaining relatively low, indicating that particle density has little influence on particle displacement. However, as the particle size increases, the displacement increases significantly from 2.308791% to 67.078761%, far surpassing the influence of density variation on displacement, thus demonstrating that particle size has a considerable effect on displacement in the jet flow model. Furthermore, changes in fluid velocity also have a pronounced impact on particle displacement, with the displacement increasing from 1.435916% to 27.681380%, indicating that fluid velocity is an important factor influencing particle displacement.

The displacement of particles with different particle sizes, densities, and fluid velocities in the swirling flow model is shown in Table 8.

Table 8. Particle displacement in the swirling flow model.

Particle Density/(kg/m^3)	Particle Diameter/(μm)	Fluid Velocity/(m/s)	Displacement/(%)
1200	10	1	1.931364
3600	10	1	2.088242
6000	10	1	2.099938
7850	10	1	2.108878
7850	1	1	1.926243
7850	10	1	2.108878
7850	50	1	6.260705
7850	100	1	13.794641
7850	150	1	145.087068
7850	10	0.1	2.015382
7850	10	1	2.108878
7850	10	10	7.627452
7850	10	30	18.044591
7850	10	50	28.587641

Under swirling flow conditions, the variation in particle density also has a minor effect on displacement. The displacement increases from 1.931364% to 2.108878%, with the overall displacement remaining relatively low, indicating that particle density has little influence on particle displacement. However, as the particle size increases, the displacement increases significantly from 1.926243% to 145.087068%, far exceeding the effect of density variation on displacement. This demonstrates that particle size has the primary influence on displacement and is much higher than the displacement in both the laminar and jet flow models, suggesting that the flow state in the swirling model has a more pronounced effect on particle displacement. Additionally, changes in fluid velocity also have a noticeable impact on particle displacement, with the displacement increasing from 2.015382% to 28.587641%, indicating that fluid velocity is also an important factor influencing particle displacement.

Overall, particle size has the most significant effect on displacement, followed by fluid velocity, while the impact of density variation is relatively small.

5. Experimental Research

5.1. Experimental Models

The experimental model is obtained through geometric similarity. The fluid velocity of the experimental model can be calculated through Reynolds number similarity, and the particle density of the experimental model can be calculated through Stokes number similarity. The corresponding parameters for the flow field simulation model and the experimental model are shown in Table 9. The corresponding parameters for the particle density of the simulation model and the experimental model are shown in Table 10. The corresponding parameters for the particle size of the simulation model and the experimental model are shown in Table 11. Here, *Exp.* and *Sim.* denote the experimental model and the simulation model, respectively. The parameters expressed as *Exp./Sim.* in Tables 9–11 represent the ratios of the corresponding parameters of the experimental model to those of the simulation model, including the geometric scale ratio, Stokes number ratio, and Reynolds number ratio.

Table 9. Corresponding parameters of the simulation model and the experimental model based on similarity theory.

Model	Inlet Dimension	Geometric Scale Ratio (*Exp./Sim.*)	Stokes Number Ratio (*Exp./Sim.*)	Reynolds Number Ratio (*Exp./Sim.*)	Density (kg/m^3)	Inlet Velocity (m/s)			Inlet Flow Rate (mL/min)		
Laminar Flow Simulation	3	10	1	1	871	1	10	30			
Laminar Flow Experiment	30				1000	0.002188	0.02188	0.06565	19.69	190.6	540.8
Jet Flow Simulation	3	10	1	1	871	1	10	30			
Jet Flow Experiment	30				1000	0.002188	0.02188	0.06565	19.69	190.6	540.8
Swirling Flow Simulation	1	10	1	1	871	10	30	50			
Swirling Flow Experiment	10				1000	0.02188	0.06565	0.10942	32.8	98.5	164.1

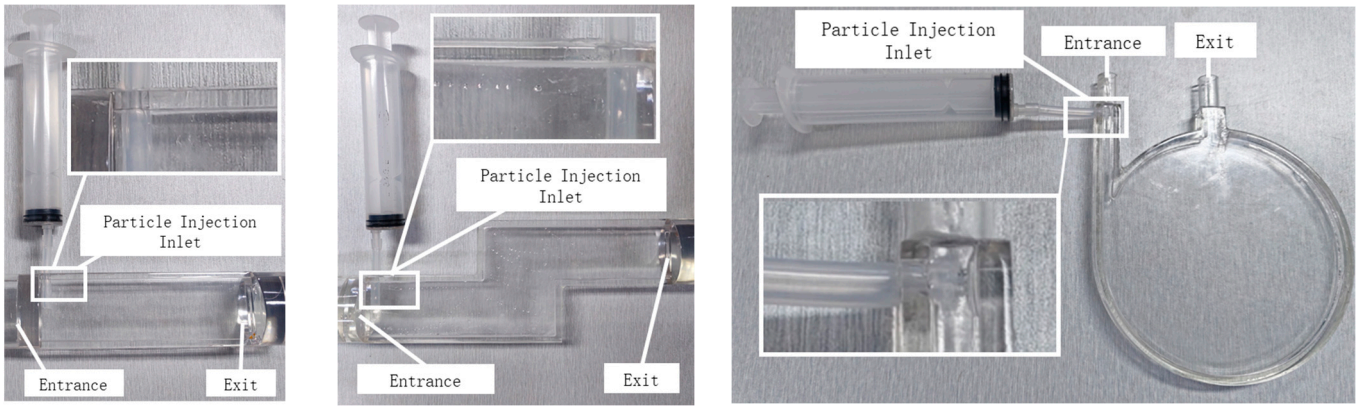
Table 10. Corresponding particle density parameters between the simulation model and the experimental model.

Model	Characteristic Length	Stokes Number Ratio (*Exp./Sim.*)	Reynolds Number Ratio (*Exp./Sim.*)	Particle Density/(kg/m^3)			
Simulation	10	1	1	1200	3600	6000	7850
Experiment				342.7788	1028.33638	1713.89396	2242.344

Table 11. Corresponding particle diameter parameters between the simulation model and the experimental model.

Model	Characteristic Length	Stokes Number Ratio (*Exp./Sim.*)	Reynolds Number Ratio (*Exp./Sim.*)	Particle Diameter/(μm)				
Simulation	10	1	1	1	10	50	100	150
Experiment				20	200	1000	2000	3000

In this experiment, the transparent acrylic material was precisely processed using 3D printing technology to create three typical flow field models: laminar, jet, and swirling flow. All three models have side holes at the inlet, connected to a particle injection device, where particles are slowly pushed to the center of the model's inlet through a hose. The laminar flow experimental model is shown in Figure 15a. The left side is the fluid inlet, connected to the inlet pipe, and the right side is the fluid outlet, connected to the outlet pipe. The jet flow experimental model is shown in Figure 15b. The left side is the fluid inlet, connected to the inlet pipe, and the right side is the fluid outlet, connected to the outlet pipe. The swirling flow experimental model is shown in Figure 15c. The left side is the fluid inlet, connected to the inlet pipe, and the right side is the fluid outlet, connected to the outlet pipe.



(**a**) (**b**) (**c**)

Figure 15. Experimental model. (**a**) Laminar flow experimental model; (**b**) Jet flow experimental model; (**c**) Swirling flow experimental model.

The particles used are aluminum spheres with a density of 2200 kg/m^3. The density of the aluminum spheres corresponds to 2242.344 kg/m^3 in the simulation model, which is calculated through similarity theory, with an error of 1.924727%. This density is acceptable for experimental analysis. Aluminum sphere particles with diameters of 0.5 mm, 0.8 mm, and 1 mm were selected.

The motion of the flow field of the experimental model is recorded and analyzed by the PIV test system, which consists of a high-speed camera, a laser, and a computer. The system shines the laser to a certain plane of the flow field, and the image of the tracer particles in that plane can be captured by the high-speed camera. Through the image-processing algorithm to analyze the same particles in the two images of the particle position, based on the position of the particle changes, combined with the time interval, you can calculate the velocity of each particle, so as to get the velocity of the flow field in the position and the flow field flow state. The experimental principle to build the experimental table is shown in Figure 16. Speed Sense Lab 310 camera 1MP3260 fps, 12GB, Output wavelength: 527 nm, repetition rate: 0.2 kHz–10 kHz, output energy: ≥20 mJ @ 1 kHz, pulse width: ~220 ns @ 1 kHz.

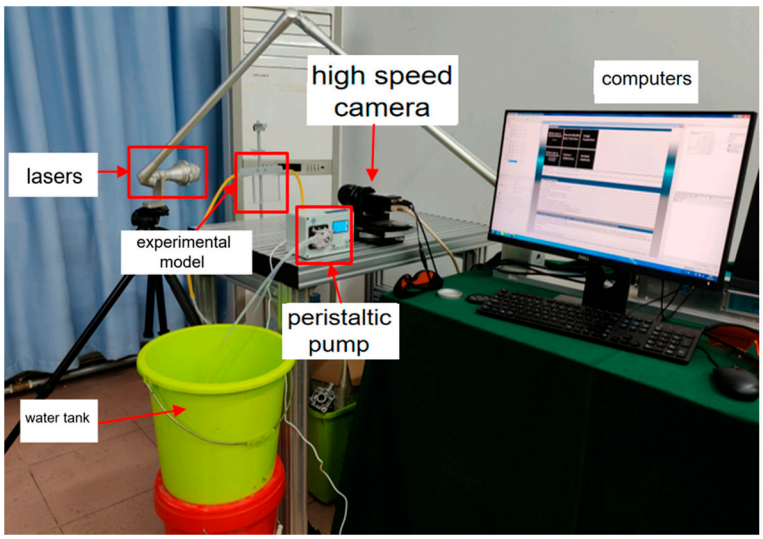


Figure 16. High-speed visualization test bench for slide valve gap flow field.

Particle Image Velocimetry (PIV) is based on introducing tracer particles with an appropriate concentration into the flow field. These particles can follow the fluid motion

well and therefore represent the motion of the corresponding fluid elements. By recording particle images at different instants with a high-speed camera and analyzing the displacement of the tracer particles over a known time interval, the velocity vectors of the flow field can be obtained through image-processing algorithms. This method is useful for analyzing flow structures such as velocity distribution and vortex evolution.

The PIV system used in this study mainly consisted of a laser source, a high-speed camera, a tracer-particle flow field, a synchronization controller, and a computer, as shown in Figure 17. The laser source emitted a sheet beam to illuminate the measurement plane of the flow field. The tracer particles scattered the light, enabling the particle distribution in the illuminated plane to be captured. The high-speed camera was arranged perpendicular to the laser sheet and continuously recorded the particle images at preset time intervals. The acquired image data were then transmitted to the computer for subsequent processing and analysis.

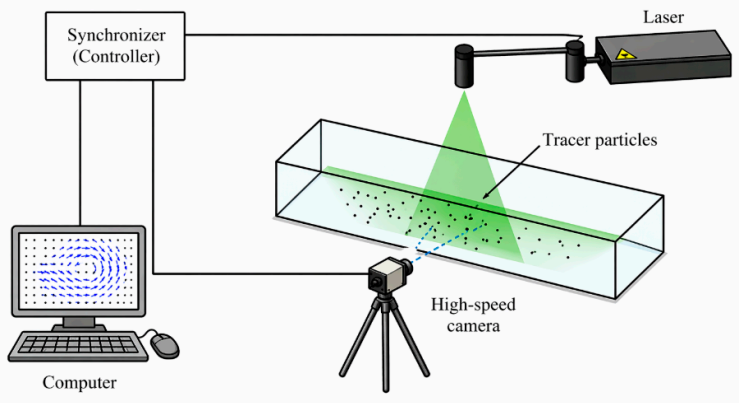


Figure 17. Schematic diagram of the basic structure of the PIV system.

5.2. Experimental Flow Field Characteristics Analysis

The velocity distribution of the three experimental model flow fields obtained from the PIV experiments is shown. The cloud plot of the laminar flow model is presented in Figure 17.

From Figure 18, it is clearly observed that the flow field exhibits distinct laminar characteristics. The streamlines are evenly distributed, and the direction is well-ordered. The streamlines in the figure are generally arranged in parallel, and the change in the direction of the velocity vectors is small, indicating that the fluid flow is stable. The variation in the velocity gradient is relatively uniform, with no significant velocity fluctuations or vortex structures. This suggests that the flow is in a stable laminar state under low Reynolds number conditions. This flow field characteristic is highly consistent with the streamline trend of the laminar flow simulation model, indicating that the flow state under the experimental conditions matches the theoretical characteristics of laminar flow.

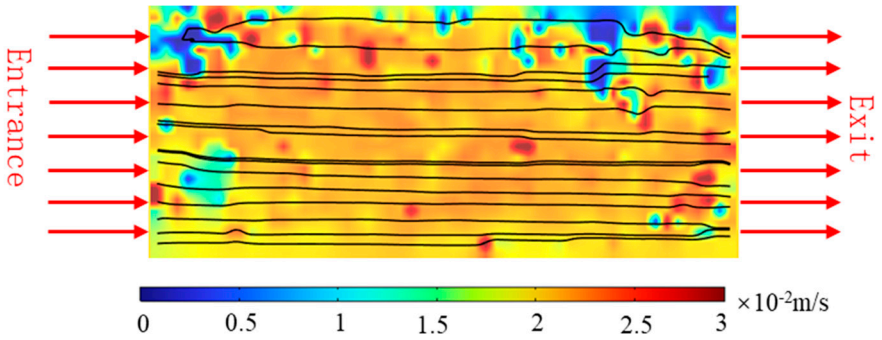


Figure 18. PIV-captured laminar flow field diagram.

The cloud plot of the jet flow model captured by the PIV experiment is shown in Figure 19.

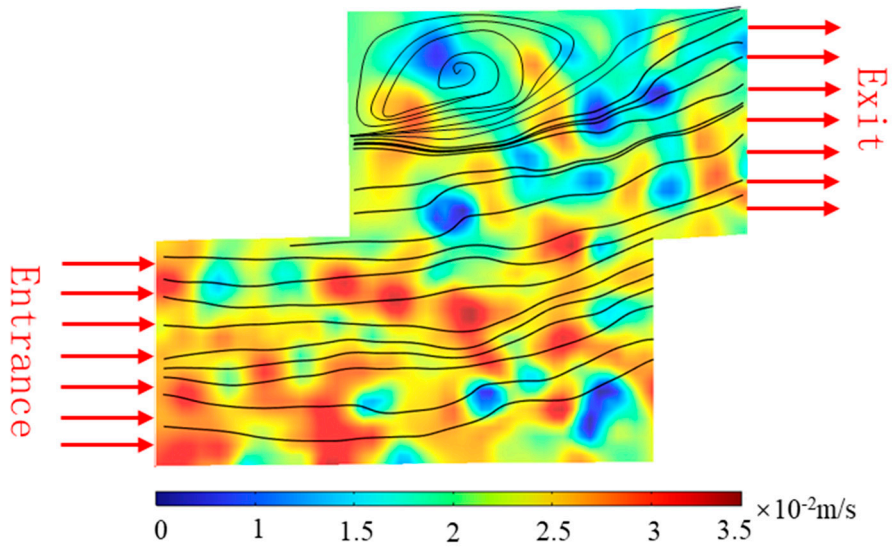


Figure 19. PIV-captured jet flow field diagram.

From Figure 19 it can be observed that at the inlet of the experimental model, the flow field velocity is relatively high. As the fluid passes through the bend, the velocity changes, and a vortex region forms above the bend. Comparing with the simulation model streamlines, it can be seen that the two are generally consistent, indicating that under the current experimental conditions, the flow state of the jet is in good agreement with the theoretical characteristics of a jet flow.

The cloud plot of the swirling flow model captured by the PIV experiment is shown in Figure 20.

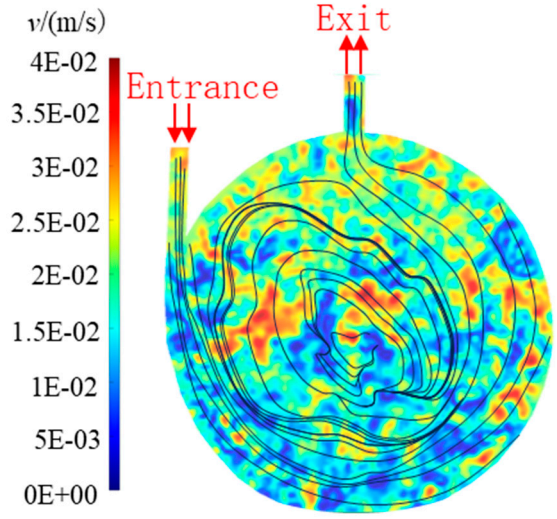


Figure 20. PIV-captured swirling flow field diagram.

From Figure 20, it can be observed that the flow field velocity at the inlet of the experimental model is relatively high, and a distinct vortex is formed after the fluid enters the circular region. The highest velocity area is located near the inlet, which roughly matches the streamlines of the simulation model, indicating that under the experimental conditions, the flow state of the swirling flow is consistent with the theoretical characteristics of swirling flow.

5.3. Comparison of Theoretical Analysis and Experimental Results

Particles are released at the center position of the model inlet, and the peristaltic pump is adjusted to the three flow rates obtained through similarity calculations, namely 19.69 mL/min, 190.6 mL/min, and 540.8 mL/min. The movement trajectories of 1 mm particles under different flow rates, or different fluid velocities, are observed. Figure 21 shows the movement trajectories of 1 mm particles under different flow rate conditions at the inlet of the laminar flow model.

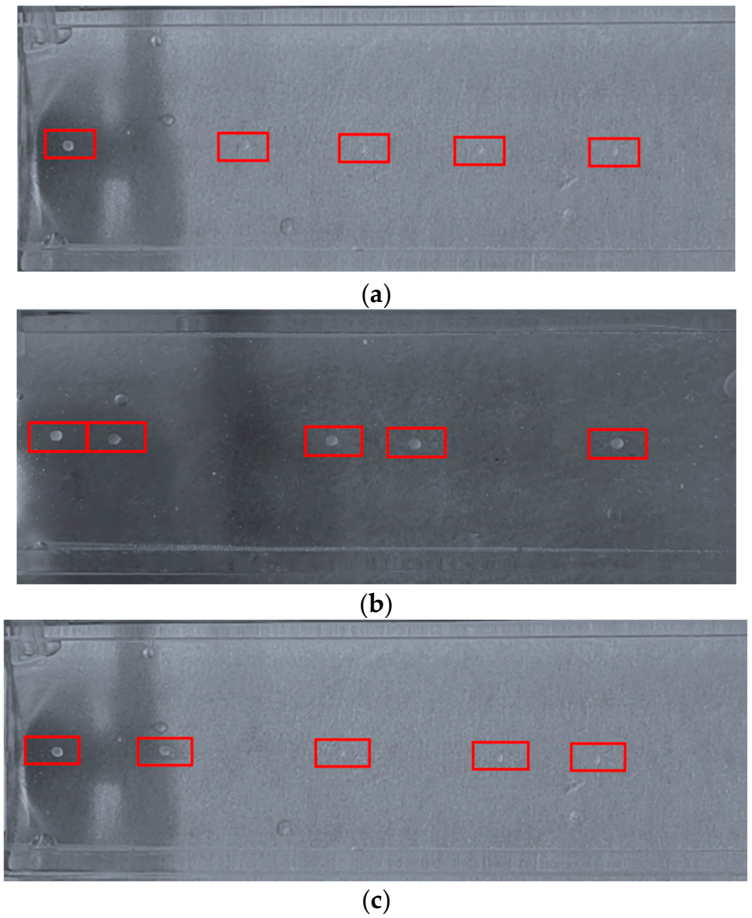


Figure 21. Movement trajectory of 1 mm particles at different flow rates. (**a**) Inlet flow rate of 19.69 mL/min; (**b**) Inlet flow rate of 190.6 mL/min; (**c**) Inlet flow rate of 540.8 mL/min.

By connecting the particle positions at each time step, a complete trajectory can be obtained. Combined with the flow field streamline diagram, the particle motion can be analyzed. At different flow velocities, by comparing the actual particle movement trajectory with the streamline diagram of the flow field, the displacement distance of the particles relative to the streamline at the same position can be calculated. The displacement distance of particles at different flow velocities is shown in Figure 22. The red color represents the experimental data for the particles, while the black color represents the simulation data. It is evident that the trends of both are consistent, exhibiting a nonlinear growth.

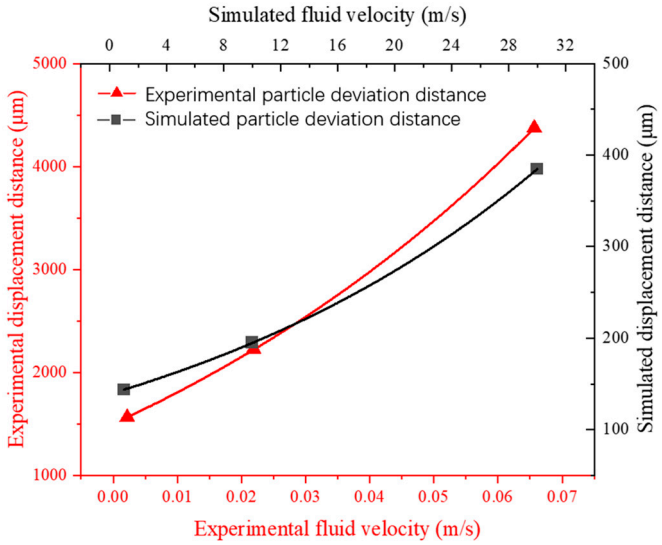


Figure 22. Variation in particle displacement distance with flow velocity.

Based on similarity theory, the displacement distance and displacement amount of the particles in the experiment and simulation under the corresponding conditions are calculated. The displacement amounts obtained from the experiment and simulation are compared, and the error between the two is calculated. The results are shown in Table 12. The simulation–experiment comparison was conducted under the selected validation particle conditions.

Table 12. Comparison of simulation and experimental models at different flow velocities.

Variables	Value		
Simulation inlet velocity (m/s)	1	10	30
Simulation displacement distance (μm)	143.753793	195.372896	384.848544
Simulation displacement (%)	4.791793	6.5124299	12.8282848
Experimental inlet velocity (m/s)	0.002188	0.02188	0.06565
Experimental displacement distance (μm)	1564.8384	2225.7876	4375.0845
Experimental displacement (%)	5.216128	7.419292	14.583615
Error (%)	8.855453	13.925096	13.683281

Analysis of Table 12 shows that as the inlet velocity increases, the displacement distance in both the simulation and experiment increases significantly. For example, when the inlet velocity increases from 1 m/s to 30 m/s (with the experimental range from 0.002188 m/s to 0.06565 m/s), the displacement in the simulation increases from 143.753793 μm to 384.848544 μm, and the displacement in the experiment increases from 1564.8384 μm to 4375.0845 μm. Both trends are consistent, with the error being less than 15%, the simulation model is able to reasonably capture the motion characteristics and deviation behavior of particles in the flow field. Although the deviation distance shows errors within an acceptable range, there is still room for improvement. Possible sources of these discrepancies include the simplified assumptions in the simulation model, measurement errors in the experimental conditions, and the complexity of forces acting on particles in the flow. Nevertheless, these results validate the effectiveness of the simulation model.

6. Conclusions

This study systematically investigates the motion characteristics of solid particles in flow fields and the mechanism of particle intrusion into the spool valve clearance. By analyzing the forces acting on the particles in the liquid phase flow field, the differences in forces between laminar and non-laminar flow fields are clarified. In laminar flow, particles are mainly affected by gravity, buoyancy, and drag force; in non-laminar flow, additional forces such as pressure gradient force, inertial force, added mass force, Magnus force, Basset force, and Saffman force must also be considered. The particle motion equation, based on Newton's second law, shows that particle movement is influenced by fluid velocity, particle diameter, and density, among other factors.

The study systematically analyzes the influence of particle density, particle size, and fluid velocity on particle displacement behavior under three typical flow states: laminar, jet, and swirling flow. The results of the study indicate:

The influence of particle size on particle displacement behavior is the most significant. In the laminar flow model, the displacement increases significantly from 0.348667% to 30.646667%; in the jet flow model, it increases from 2.308791% to 67.078761%; and in the swirling flow model, it rises from 1.926243% to 145.087068%. The results show that particle size is the dominant factor in determining the degree of particle displacement.

Fluid velocity also has a noticeable impact on particle displacement. As the velocity increases, the displacement in laminar flow increases from 0.156966% to 1.781229%; in jet flow, it increases from 1.435916% to 27.681380%; and in swirling flow, it increases from 2.015382% to 28.587641%. This indicates that fluid velocity plays an important role in altering the inertial trajectory of particles, particularly in high-energy flow fields.

The effect of particle density variation on displacement is relatively small. In all three flow states, the increase in displacement caused by density variation is limited. For example, in laminar flow, the displacement only increases from 0.193642% to 0.549837%, indicating that, under the same conditions, particle density has less influence on displacement behavior compared to particle size and velocity factors.

The particle displacement in the swirling flow model is the most drastic, far exceeding that of laminar and jet flow states. This is primarily due to the significant centrifugal force and the relatively complex structure in swirling flow, which further amplifies the effect of particle size and velocity on particle motion trajectories.

In conclusion, particle displacement behavior is primarily controlled by particle size and fluid velocity, with particle density having a secondary effect. The results of this study provide theoretical support for predicting and controlling particle transport behavior in servo valves, with promising applications, especially in fuel injection, microfluidics, and particle separation systems.

Compared with existing studies that mainly focus on fully three-dimensional simulations or erosion and wear mechanisms in specific valve geometries, the present study aims to extract general particle migration characteristics under different representative flow-field types. By combining simplified numerical models with experimental flow-field validation, this work provides a complementary understanding of particle behavior relevant to servo valve contamination problems. It should be noted, however, that the present representative flow fields are established based on simplified two-dimensional models, which are mainly intended to capture the dominant flow features and general particle migration trends. The actual spool–sleeve flow field is inherently three-dimensional, and effects related to clearance variation, edge structures, and local geometric complexities may further influence particle transport behavior. Therefore, a full three-dimensional model will be considered in future work to provide a more comprehensive description of the underlying physics.

The present study focuses on particle migration characteristics in several representative valve-like flow fields. However, practical spool–sleeve flows may also enter transitional and turbulent regimes under certain geometric and operating conditions. These more complex regimes may further affect particle dispersion, deposition, and trajectory evolution. Therefore, future work will extend the present analysis to transitional and turbulent flow conditions, combined with more realistic valve geometry and appropriate turbulence/transition modeling, in order to provide a more comprehensive understanding of particle transport in servo valves. In the present study, the effects of particle surface properties, shape factors, and material differences are not considered. Future work will incorporate more realistic particle characteristics to further improve the physical fidelity of the model. In the present study, particle transport is analyzed under a dilute-particle assumption. Therefore, particle–particle interaction effects, such as collision, agglomeration, and clustering, are neglected, and the analysis focuses on the dominant influence of fluid–particle interaction on particle migration behavior. These interaction effects will be considered in future work under higher-concentration and more realistic contamination conditions. In the present simulations, particles were released from the inlet center with an initial velocity of 0 m/s. This assumption was introduced as a unified initial condition for comparative analysis of particle migration under different representative flow fields, rather than as an exact description of the inlet kinematics in a real valve. Therefore, the reported displacement results should be interpreted as relative migration characteristics under a controlled initial condition. More realistic inlet particle velocities and stronger coupling effects will be considered in future work.

Author Contributions: Methodology, J.Z. and R.D.; software, J.W. and R.D.; validation, J.Z. and R.D.; data curation, Y.S.; resources, Y.L. and X.K.; formal analysis, R.D.; writing—original draft preparation, R.D. and Y.S.; writing—review and editing, J.Z., R.D. and Y.S. All authors have read and agreed to the published version of the manuscript.

Funding: This research was funded by the National Natural Science Foundation of China, grant number 52275068. This research was funded by the Open Foundation of the State Key Laboratory of Taihang Laboratory, grant number QTJLHT202404090002. This research was funded by the industry-university-research cooperation project of Aviation Engine Corporation of China, grant number HFZL2024CXY014.

Data Availability Statement: The original contributions presented in this study are included in the article. Further inquiries can be directed to the corresponding author.

Conflicts of Interest: The research was conducted in the absence of any commercial or financial relationships that could be construed as a potential conflict of interest.

References

1. Jiao, Z.X.; Wu, S.; Li, Y.; Zhang, C.; Jin, H.T.; Shu, S.; Wei, R.L.; Li, R.J.; Wang, Y.; Zhang, H.Y.; et al. Development Status and Trends of the Intelligence of Hydraulic Components and Systems. *J. Mech. Eng.* **2023**, *59*, 357–384.
2. Liu, Q.X.; Liu, F.; Ji, H.; Li, N.; Wang, C.; Lin, G. Particle erosion transient process visualization and influencing factors of the hydraulic servo spool valve orifice. *Flow Meas. Instrum.* **2023**, *89*, 102273. [CrossRef]
3. Singh, M.; Lathkar, G.S.; Basu, S.K. Failure prevention of hydraulic system based on oil contamination. *J. Inst. Eng. Ser. C* **2012**, *93*, 269–274. [CrossRef]
4. Zhang, H.P.; Huang, W.; Zhang, Y.D.; Shen, Y.; Li, D.Q. Design of the microfluidic chip of oil detection. *Appl. Mech. Mater.* **2012**, *117*, 517–520. [CrossRef]
5. Zhu, G.; Zhao, Y.; Wang, Z.; Khalid, M.-S.; Liu, M. Semi-resolved CFD-DEM simulation of fine particle migration with heat transfer in heterogeneous porous media. *Int. J. Heat Mass Transf.* **2022**, *197*, 123349. [CrossRef]
6. Brazhenko, V.; Mochalin, I. Terminal velocity and drag coefficient of a smooth steel sphere moving in the water-filled vertical and inclined glass pipe (Newton regime). *Powder Technol.* **2024**, *446*, 120120. [CrossRef]

7. Yang, Z.; Lian, X.; Savari, C.; Barigou, M. Evaluating the effectiveness of CFD-DEM and SPH-DEM for complex pipe flow simulations with and without particles. *Chem. Eng. Sci.* **2024**, *288*, 119788. [CrossRef]
8. Daghooghi, M.; Borazjani, I. The effects of irregular shape on the particle stress of dilute suspensions. *J. Fluid Mech.* **2018**, *839*, 663–692. [CrossRef]
9. Terrell, E.J.; Higgs, C.F., III. A modeling approach for predicting the abrasive particle motion during chemical mechanical polishing. *J. Tribol.* **2007**, *129*, 933–941. [CrossRef]
10. Romero-Valle, M.A.; Goniva, C.; Nirschl, H. Modeling of non-spherical particle flows: Movement and orientation behavior. *Powder Technol.* **2021**, *382*, 351–363. [CrossRef]
11. Fedina, T.; Sundqvist, J.; Kaplan, A.F.H. The role of powder morphology in particle movement behavior in laser powder bed fusion with an emphasis on fluid drag. *Powder Technol.* **2022**, *395*, 720–731. [CrossRef]
12. Naghashnejad, M.; Lin, Y.T.; Panides, E.; Banerjee, J.; Kim, S.H.; Borhan, A. Hydrodynamic force on a hemispheroidal particle attached to a planar surface in linear shear flow. *Powder Technol.* **2024**, *434*, 119352. [CrossRef]
13. Robinson, M.; Ramaioli, M.; Luding, S. Fluid-particle flow simulations using two-way-coupled mesoscale SPH-DEM and validation. *Int. J. Multiph. Flow* **2014**, *59*, 121–134. [CrossRef]
14. Ebrahimi, M.; Gupta, P.; Robinson, M.; Crapper, M.; Ramaioli, M.; Ooi, J.Y. Comparison of coupled DEM-CFD and SPH-DEM methods in single and multiple particle sedimentation test cases. In *PARTICLES III: Proceedings of the III International Conference on Particle-Based Methods: Fundamentals and Applications*; CIMNE: Barcelona, Spain, 2013; pp. 322–334.
15. Kandlikar, S.G.; Schmitt, D.; Carrano, A.L.; Taylor, J.B. Characterization of surface roughness effects on pressure drop in single-phase flow in minichannels. *Phys. Fluids* **2005**, *17*, 100606. [CrossRef]
16. Tic, V.; Lovrec, D. Trajectories of solid and gaseous particles in a hydraulic reservoir. In Proceedings of the 8th International Fluid Power Conference IFK, Dresden, Germany, 26–28 March 2012.
17. Elaswad, R.; El-Sheimy, N.; Mohamad, A. Trajectory dynamics of particles in accelerated toroidal pipe: A computational study using CFD-DPM simulations. *J. Comput. Sci.* **2024**, *78*, 102285. [CrossRef]
18. Pomeroy, P.E. Erosive Wear Failure of Spool Valves. Ph.D. Thesis, University of Bath, Bath, UK, 1995.
19. Vaughan, N.D.; Pomeroy, P.E.; Tilley, D.G. The contribution of erosive wear to the performance degradation of sliding spool servo valves. *Proc. Inst. Mech. Eng. Part J J. Eng. Tribol.* **1998**, *212*, 437–451. [CrossRef]
20. Edwards, J.K. Development, Validation, and Application of a Three-Dimensional, CFD Base Erosion Prediction Procedure. Ph.D. Thesis, The University of Tulsa, Tulsa, OK, USA, 2000.
21. Frawley, P.; Corish, J.; Niven, A.; Geron, M. Combination of CFD and DOE to analyse solid particle erosion in elbows. *Int. J. Comput. Fluid Dyn.* **2009**, *23*, 411–426. [CrossRef]
22. Maxey, M.R.; Riley, J.J. Equation of motion for a small rigid sphere in a nonuniform flow. *Phys. Fluids* **1983**, *26*, 883–889. [CrossRef]
23. Clift, R.; Grace, J.R.; Weber, M.E. *Bubbles, Drops, and Particles*; Dover Publications, Inc.: Mineola, NY, USA, 2013.
24. Saffman, P.G. The lift on a small sphere in a slow shear flow. *J. Fluid Mech.* **1965**, *22*, 385–400. [CrossRef]

Disclaimer/Publisher's Note: The statements, opinions and data contained in all publications are solely those of the individual author(s) and contributor(s) and not of MDPI and/or the editor(s). MDPI and/or the editor(s) disclaim responsibility for any injury to people or property resulting from any ideas, methods, instructions or products referred to in the content.